Discovery of giant and conventional magnetofossils bookending Cretaceous Oceanic Anoxic Event 2

Check for updates

Courtney L. Wagner [1] ✉, Ioan Lascu [1], Jean M. Self-Trail[2], Tim Gooding[1], Kenneth J. T. Livi[3], Gianna Greger[4], Kristina Gardner[2], Jody Wycech [5], Mark Dreier[5] & Tom Oliver[5]

Conventional magnetofossils are the remains of magnetotactic bacteria and giant magnetofossils are the remains of iron biomineralizing organisms that have not yet been identified. We report the oldest robust conventional and giant magnetofossil records, ~97 Ma, from marine sediments drilled in Holland Park, Virginia, USA. The Holland Park core records the Cenomanian-Turonian boundary and Oceanic-Anoxic Event 2 (OAE2). Magnetic datasets indicate single domain magnetite within the clay-rich sediments bookending OAE2. Electron microscopy images from these intervals highlight conventional and giant magnetofossil morphologies, including three potentially new giant magnetofossil morphologies: seeds, squash, and spades. There is an overall high abundance and morphological disparity of magnetofossils at Holland Park. However, we observe abundance, disparity, and preservation changes between the magnetofossil assemblages bookending OAE2. Our observations provide clues toward understanding the ecological thresholds of the enigmatic organisms that produce giant magnetofossils and evidence that magnetofossils may be widely distributed in the geologic record.

Magnetotactic bacteria (MTB) biomineralize iron nanoparticles that they use to navigate between specific redox conditions in aquatic environments[1–5]. Most MTB inhabit microaerobic environments within the water column or sediments, within or just below the oxic–anoxic interface[5]. MTB play a key role in the iron cycle by sequestering iron as biogenic magnetite or greigite. These minerals are either consumed by other organisms, dissolved back into the water column, or preserved as magnetic nanofossils (conventional magnetofossils)[6–8].

MTB are also involved in sulphur, nitrogen, silicon, phosphorous and carbon cycling[9–13]; studies even suggest that iron and carbon are limiting factors for MTB metabolism[14,15]. MTB are diverse organisms found globally in a wide range of habitats, including harsh environments such as acid mine drainages and acidic lagoons[9,16,17]. Molecular studies suggest that MTB may have evolved as early as the Archaean[18]. As such, MTB fossils may fingerprint life in these habitats and may play an important, yet underexplored, role in aquatic biogeochemical cycles throughout Earth history.

The distinct magnetic and crystallographic properties of magnetofossils make them straightforward to detect within bulk sediment samples.

These attributes make magnetofossils excellent biomarkers for life and redox geochemistry in the geologic record[19,20]. Putative conventional magnetofossils were reported in stromatolites from 2.7 Ga and cherts from 2 Ga in Western Australia[21,22], but they do not meet the robust criteria for characterising magnetofossils which combines, at minimum, robust morphologic, crystallographic, and magnetic datasets[14,20,23–25]. The oldest irrefutable evidence for conventional magnetofossils dates to the mid-Cretaceous[26,27]. Numerous younger, compelling conventional magnetofossil records have been described beyond these reports.

In contrast to the small size of conventional magnetofossils (~20–120 nm), giant magnetofossils are unusually large (>1 μm) magnetite crystals with putative biologic origin[28–30]. The organisms responsible for their biomineralization have not yet been recognised and are here referred to as giant iron-biomineralizing organisms (GIBO). Until recently, giant magnetofossils have only been identified from sediments surrounding Eocene hyperthermal events with evidence for increased water-column stratification, deoxygenation, iron delivery and organic matter supply; therefore, giant magnetofossils have been considered a proxy for

[1]Department of Mineral Sciences, National Museum of Natural History, Smithsonian Institution, 1000 Constitution Ave NW, Washington, DC, 20560, USA. [2]U.S. Geological Survey, Florence Bascom Geoscience Center, 12201 Sunrise Valley Dr., 926A National Center, Reston, VA, 20192, USA. [3]Materials Characterization and Processing, Department of Materials Sciences and Engineering, Johns Hopkins University, 800 Wyman Park Drive, Baltimore, MD, 21211, USA. [4]Department of Geology and Environmental Geosciences, Lafayette College, 730 High St., Easton, Easton, PA, 18042, USA. [5]U.S. Geological Survey, Central Energy Resources Science Center, Denver Federal Center, Box 25046, MS939, Denver, CO, 80225, USA. ✉e-mail: courtneywagner.geo@gmail.com

environmental changes during these events[28–32]. Recent studies report giant magnetofossil assemblages spanning the last ~93 Ma–1.8 ka[27,33,34]. Notably, these studies include global cooling periods. Nonetheless, widespread MTB distribution in the oceans (both in the modern and fossil record)[9,14], where iron is limited, and the proliferation of marine giant magnetofossils during large-scale changes to hydrological and biogeochemical cycles, suggests that MTB and GIBO can be tied to the marine iron cycle. For these reasons, an improved understanding of magnetofossil distribution in the geologic record may have implications for reconstructing iron cycle changes during climatic events.

In this study, we report the oldest robust conventional and giant magnetofossil assemblages in marine sediments found to date from the mid-Cretaceous Cenomanian and Turonian stages (~97 Ma). These sediments bookend Oceanic Anoxic Event 2 (OAE2), a major carbon cycle perturbation marked by a positive carbon isotope excursion. Sediments were collected from the Holland Park core, VA, USA, and were deposited in a continental shelf environment (Fig. 1). The magnetofossil assemblages presented here are exceptionally well-preserved and display a variety of morphologies (high disparity) consistent with previously documented conventional and giant magnetofossil shapes. In addition to standard magnetofossil morphologies, we describe three potentially new or previously undocumented giant magnetofossil crystal shapes. Here, we describe these magnetofossils and discuss their implications for understanding the ecological thresholds and preferences of these organisms. This information, combined with the straightforward, cost-effective, non-invasive magnetic detection of magnetofossils, underscores their usefulness as environmental proxies.

Results

Stratigraphy of the Holland Park core

The study of Cenomanian to Turonian sediments in the Atlantic Coastal Plain is limited to the small number of cores available. Sequence stratigraphy and sedimentology suggest that these sediments were deposited in a shoreline-proximal shelf environment[35,36] and that they represent the latest Cenomanian-earliest Turonian sea level rise before the early Turonian highstand event. While sediments of this age have been documented as belonging to the Clubhouse and Sunny Point formations in South and North Carolina[35–39], placement within a specific lithostratigraphic formation in Virginia is uncertain. Previously, documentation of Cenomanian sediments from the mid-Atlantic has been restricted to one sample from the E.G. Taylor no. 1-G well, eastern shore of Virginia[40]; there has been no

Fig. 1 | Location map for the Holland Park core. Present-day map of southeast Virginia, USA. The location of the Holland Park core (this study) is indicated by the red dot. This map was created using the Geographic Information System.

documentation of the Turonian. However, both lower and upper Turonian sediments are documented in North Carolina[35,38] and New Jersey[41,42] and, therefore, their presence in Virginia is unsurprising.

The Lower-Upper Cretaceous contact is at 124.7 m (Fig. 2), where the micaceous sandy clay to clayey silt of what we provisionally assign to the Clubhouse Formation unconformably overlies the mottled, sandy silty palaeosols of the Potomac Group. The age-equivalent Clubhouse sediments contain abundant shell hash material, pyrite and marcasite nodules, and intervals of organic-rich laminated black shale. Here, the presumed Clubhouse Formation becomes increasingly sandier and less clayey up-section. Dark laminated clays disappear at approximately 100 m, marking the end of OAE2, and are overlain by very fine to fine micaceous quartz sand with shell fragment interbeds. We place the Cenomanian-Turonian boundary at this point, based on biostratigraphy, as discussed below. We tentatively place the Clubhouse and Sunny Point contact at 86.9 m, where there is a decrease in mica, pyrite, and mud matrix abundance accompanied by a colour change. The top of the Turonian, which occurs at 82 m, is a major unconformity where the presumed Sunny Point Formation is overlain by the Danian Brightseat Formation.

Calcareous nannofossils were identified to the species level, and they confirm that the Holland Park sediments span the Cenomanian-Turonian boundary (Fig. 2 and Fig. S1). The basal Cenomanian contains predominantly common calcareous nannofossils. *Eiffelithus turriseiffelii*, *Gartnerago obliquum*, and *Helenia chiastia* at 124.4 m place this sample in upper Zone CC9[43] and Zone UC2[44]. The first occurrence of *Lithraphidites acutus acutus* at 120.4 m marks the base of Zone CC10a and UC3–UC4 (undifferentiated). Calcareous nannofossils become increasingly sporadic at 117.5 m, and thus, the sediments are more difficult to date. The interval from 115.5 to 102.8 m is placed tentatively in Zone UC5 based on the absence of *L. acutus acutus* and *H. chiastia*. The first occurrence of *Eprolithus moratus* and *E. octopetalus* at 98.1 m confirms the beginning of the Turonian and the base of Zone CC10b and UC6b[43–45]. The marker species for UC7, *Quadrum gartneri*, is not recorded, but this may be due to sporadic calcareous nannofossil occurrence in this interval. An unconformity most likely is present at 86.9 m, at the presumed Clubhouse-Sunny Point contact: the sediment colour change coincides with the first occurrence of Zone CC12 (UC8) species, as indicated by the presence of *Eiffelithus eximius*. Zones CC7/UC11 are either missing or not represented due to depositional palaeoenvironmental conditions. The presence of *Chiasmolithus danicus* and *Cruciplacolithus tenuis* at 82 m marks the base of the Danian; calcareous nannofossils suggest a hiatus of approximately 25.5 my in this core[46].

Total organic carbon (TOC) values shift from 0.5% to as much as 2% from 117.9 to 100.5 m, coinciding with deposition of black shales. This TOC shift also coincides with a ~2‰ positive $\delta^{13}C_{org}$ excursion from −23 to −21 in the same interval. Increased nannofossil dissolution in horizons from 117.5 to 115.7 m and 102.0 to 99.3 m is also recorded. These TOC and $\delta^{13}C_{org}$ values are similar to those recorded by Lowery et al. [36]. for Atlantic Coastal Plain cores from North Carolina, and most likely represent the global record of OAE2 (Fig. 2)[47–50].

Environmental magnetic trends and magnetic assemblages

Bulk magnetic parameters such as saturation magnetisation (M_s), saturation remanence (M_r), coercivity (B_c) and coercivity of remanence (B_{cr}) can be used to characterise average magnetic grain size variations within a sample[51]. Results from our bulk magnetic measurements have similar trends to the nannofossil assemblages at Holland Park which have distinct changes coinciding with dissolution events and OAE2 (Fig. 2). As such, these magnetic datasets may also reflect environmental changes. Generally, M_s, M_r and B_{cr}/B_c values decrease when M_r/M_s, B_c and B_{cr} values increase. This occurs at and below 125.2 m (just before the Cenomanian interval), from 117.9 to 96.7 m, and then at and above 92.3 m (continuing to the top of the core). The 117.9–96.7 m interval coincides well with the deepest and shallowest values for nannofossil dissolution horizons that mark the local extent of OAE2. First-order reversal curve (FORC) datasets for these horizons do not contain magnetic signatures consistent with the presence of
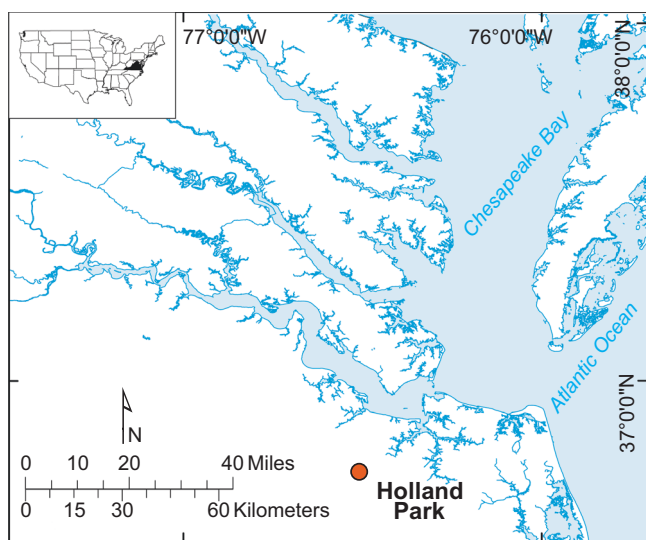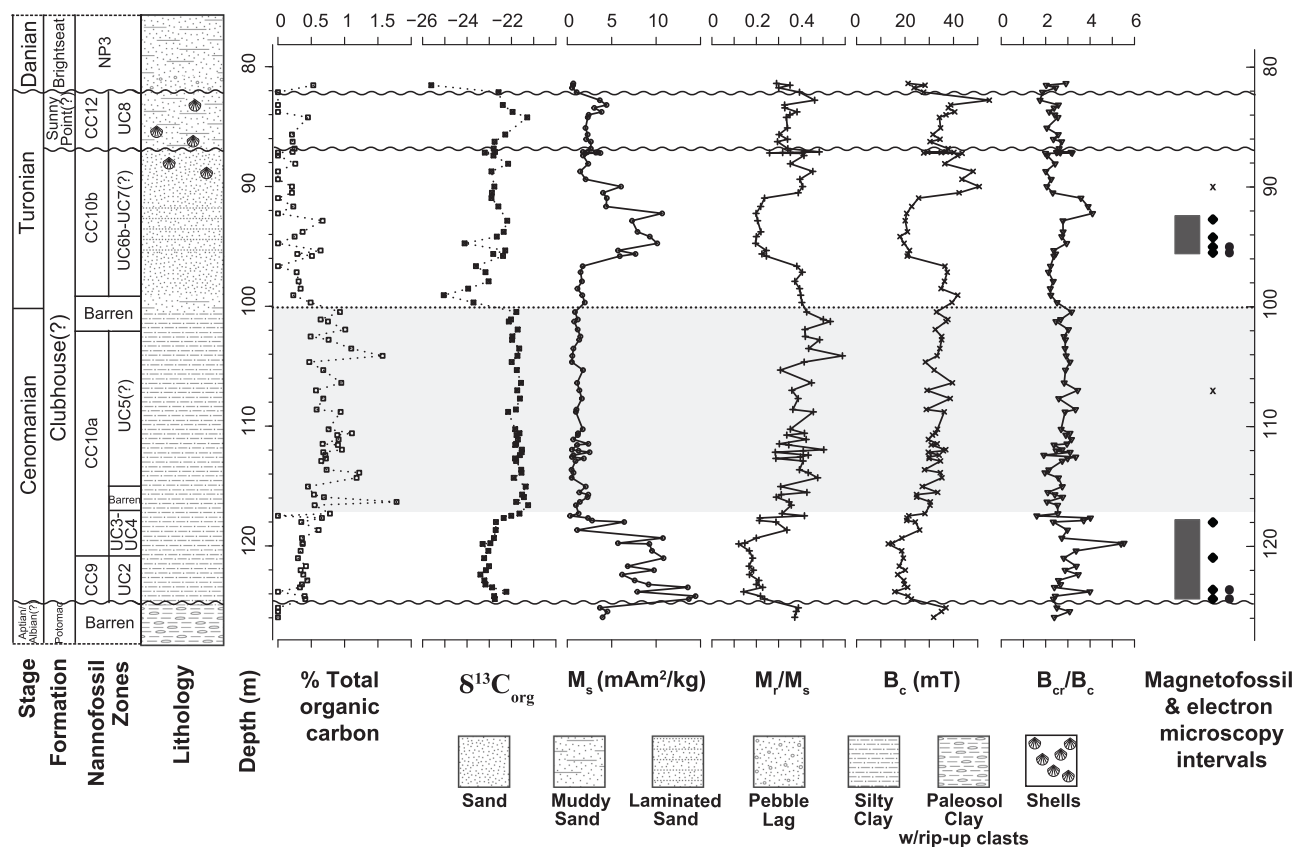
Fig. 2 | Stratigraphy of the Holland Park core. From left to right: chrono-, bio- and lithostratigraphy (zone IDs are in the Supporting Information), per cent total organic carbon, $\delta^{13}C$ from organic carbon, bulk magnetic parameters including saturation magnetisation (M_s), remanence ratio (M_{rs}/M_s), coercivity (B_c), coercivity ratio (B_{cr}/B_c), magnetofossil intervals (grey bars), and horizons selected for scanning electron microscopy (black diamonds and x-marks, left) and transmission electron microscopy (black dots, right). Magnetofossils were identified in all electron microscopy horizons except for the two non-magnetofossil horizons that are denoted with x-marks, 107.02 m and 90.01 m. The Nannofossil zones are from[43,44,46]. Oceanic Anoxic Event 2, as marked by $\delta^{13}C$ from organic carbon values, is highlighted by the grey background from 117.3 to 100.5 m. The dotted horizontal line at the top of the OAE2 interval, at 100.5 m, also demarks the Cenomanian-Turonian boundary. The three wavy lines represent unconformities: one near the bottom (124.7 m, at the Aptian/Albian(?)-Cenomanian boundary) and two near the top of the core (one at 86.9 m and the other at 82 m, at the Turonian-Danian boundary).

magnetofossils (Fig. S2)[52–54]. On the other hand, the Cenomanian interval from 124.4 to 118.0 m and the Turonian interval from 95.8 to 92.9 m are characterised by higher M_s, M_r and B_{cr}/B_c values and lower M_r/M_s, B_c and B_{cr} values. Our 22 FORC datasets from these intervals contain features that are consistent with single-domain biogenic magnetite including distinct central ridges, negative regions, and coercivity distributions with peaks between ~20 and 50 mT (Figs. 3, S3 and S4)[52–54].

Electron microscopy analyses of conventional and giant magnetofossils

SEM images of magnetic extracts from the eight stratigraphic horizons analysed (HP40825, HP40624, HP39705, HP38715, HP31435, HP31375, HP30900 and HP30465) reveal both conventional and giant magnetofossils (Figs. 4A–D, 5A–D and S5–S12). All eight imaged horizons contain conventional magnetofossil morphologies known to be produced by magnetotactic bacteria, i.e., cuboctahedra, small bullets, medium-length bullets, large bullets and prismatic crystals[31,55]. Every sample contains the four standard giant magnetofossil morphologies: giant bullets, spindles, needles and spearheads[28,30,31], except for the extract from HP31375 which did not contain giant bullets or spearheads. Energy dispersive X-ray spectroscopy confirms the presence of iron oxide minerals (Figs. S5–S12). We did not observe magnetofossils within the magnetic extracts from stratigraphic horizons HP35110 and HP29530, outside of the magnetofossil intervals, so we do not discuss them further.

Conventional magnetofossil morphologies are observed in TEM images from each of the four imaged samples (HP40825, HP40624,

HP31435 and HP31375) (Figs. 4E, 5E S13–S16). All giant magnetofossil morphologies are identified in the TEM images from extracts from HP40825 and HP31375; only giant bullets and needles are identified in HP40624, and only spearheads are identified in HP31435. Indexed selected area electron diffraction (SAED) patterns and lattice spacing calculations confirm the presence of magnetite in samples HP40825 and HP31375 (Figs. 4F, 5F and S16). In summary, we find that each of the eight stratigraphic horizons contains magnetofossil morphologies with sizes, shapes, and compositions consistent with previously reported conventional and giant magnetite magnetofossils[28,30–32]. Most notably, dimensional analysis and size comparisons of the giant magnetofossils imaged in this study show that Cretaceous giant magnetofossils fall within the same size ranges as giant magnetofossils imaged from the upper Palaeocene and lower Eocene (Fig. 6 and S17–S20)[30–32].

In addition to imaging the four known giant magnetofossil morphologies, we report further unusual particle shapes from the magnetic extracts (Figs. 6, 7 and S21–27). The most notable of these particles are the "spade", "seed", and "squash" particle morphologies. Seed-like particles (~1350 × 900 nm) are identified in a TEM image from HP40825 and SEM images from HP38715, HP31435 and HP30900. These particles have more noticeable crystal faces, an overall hexoctahedral shape, and appear to be elongated along one axis[56]. The squash-like particles are large (~2570 × 1300 nm), have less regular shapes, and are only identified in SEM images from HP30900. They resemble oblate ellipsoids that are curved on one end but have blunt stalks on the other end. These particles contain faint crystal faces parallel to particle long axes, with rougher surface textures than
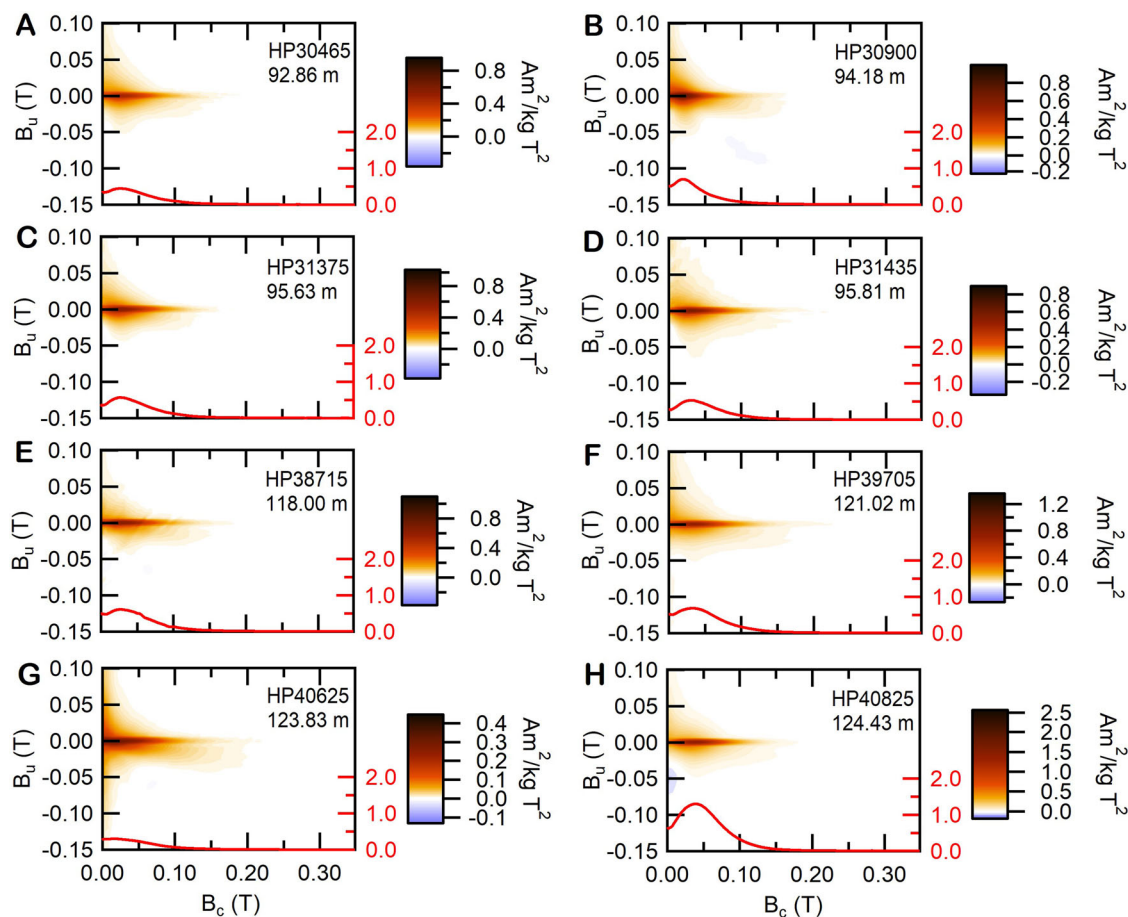
Fig. 3 | Representative first-order reversal curve (FORC) diagrams. The FORC diagrams in panels **A–D** are the representative diagrams for the post-OAE2 magnetofossil intervals that were selected for magnetic extracts and electron microscopy experiments: HP30465, HP30900, HP31375 and HP31435. The FORC diagrams in panels **E–H** are the representative diagrams for the pre-OAE2 magnetofossil intervals that were selected for magnetic extracts and electron microscopy experiments: HP38715, HP39705, HP40625 and HP40825. The red curves at the bottom of the diagrams are coercivity profiles across where $B_u = 0$ T on the FORC diagrams. Note that these datasets are mass normalised. All eight of these FORC diagrams contain features consistent with the presence of single domain magnetite: negative or low signal regions near where $B_u = -0.05$ T and $B_c = 0.01$ T, 'central ridges' where $B_u = 0$ T, and distinct central ridge contributions between approximately $B_c = 0.02$ T to $B_c = 0.05$ T[52–54,77].

the other particles. Spade-like particles (~430 × 320 nm) are identified in SEM images from HP40825, HP39705 and HP31375. Spades have uniform morphologies that are similar to giant spearheads: they have a wide centre that tapers toward a point on one end and a wider, blunter bottom on the other end. However, the spades seem to have "smoother" surfaces than giant spearheads (which tend to have "grooved girdles" around their centres) and do not have as much variety in morphology (e.g., varying lengths, widths and stalk lengths).

Our magnetic extraction, electron microscopy imaging, and magnetofossil counting procedures were consistent between stratigraphic horizons, which enables us to estimate magnetofossil abundance changes between each sample, or the actual number of counted magnetofossils. We also calculated the relative abundances of each magnetofossil category per sample. We consider two general cases: the first involves previously reported magnetofossil morphologies (i.e., all conventional and giant morphologies, excluding seed, squash and spade shapes) (Tables S1–S3) and the second combines previously reported magnetofossils with the three new morphologies described here (i.e., all conventional and giant morphologies, including squash, seed and spade putative giant magnetofossils) (Tables S4–S6). Below we describe the second case involving putative giant magnetofossils; a description of the first case without putative giant magnetofossils, can be found in the Supporting Information text.

The total conventional magnetofossil abundance decreases by ~80% after OAE2, from $n = 15,716$ to $n = 3140$, and the abundance of each conventional magnetofossil category drops by >60% (Table S4). On the other hand, the total giant magnetofossil abundance increases by ~3.5%. Moreover, there is a large drop in conventional magnetofossil abundance from the pre- to post-OAE2 intervals but minor differences in giant magnetofossil abundances. This difference in conventional and giant magnetofossil percentages coincides with a difference in preservation from pre- and post-OAE2 intervals seen in SEM images (Fig. S28). Giant magnetofossils are well preserved in both intervals, but conventional magnetofossils are less well-preserved in magnetic mineral extracts from the post-OAE2 intervals: conventional magnetofossils are sparser, and there are films on these extracts. Notably, although the giant magnetofossil percentages do not change significantly, the percent volume of magnetite giant magnetofossils increases from ~51.5% to ~96.1% due to the significant decrease in conventional magnetofossils (Tables S7–8).

We also observe a ~11.5% decrease in the relative abundance of cuboctahedral magnetofossils from the pre- to post-OAE2 intervals, a change that coincides with a ~8% increase in small bullet-shaped magnetofossils (Table S5). The abundance of the remaining conventional magnetofossil categories remains relatively constant. The percentage of conventional magnetofossils greatly outnumbers the percentage of giant

Fig. 4 | Electron micrographs of magnetofossils from the pre-OAE2 interval. A Scanning electron microscope (SEM) image of giant bullets from HP39705. **B** SEM image of a spindle from HP40625. **C** SEM image of needles from HP40825. **D** SEM image of a spearhead from HP40625 with two pronounced grooves bisecting the crystal at the widest points. **E** Transmission electron microscope image of conventional magnetofossils and a giant needle from HP40825. The black circle over the needle is the area from which the selected area electron diffraction (SAED) pattern in panel **F** was acquired. **F** The SAED pattern for the needle in **E** with the 111 and 002 magnetite reflections labelled. The red arrows in panels **A–D** point to giant magnetofossils. An example of the conventional magnetofossils that can be seen in the SEM images is highlighted by the red circle in panel (**A**).
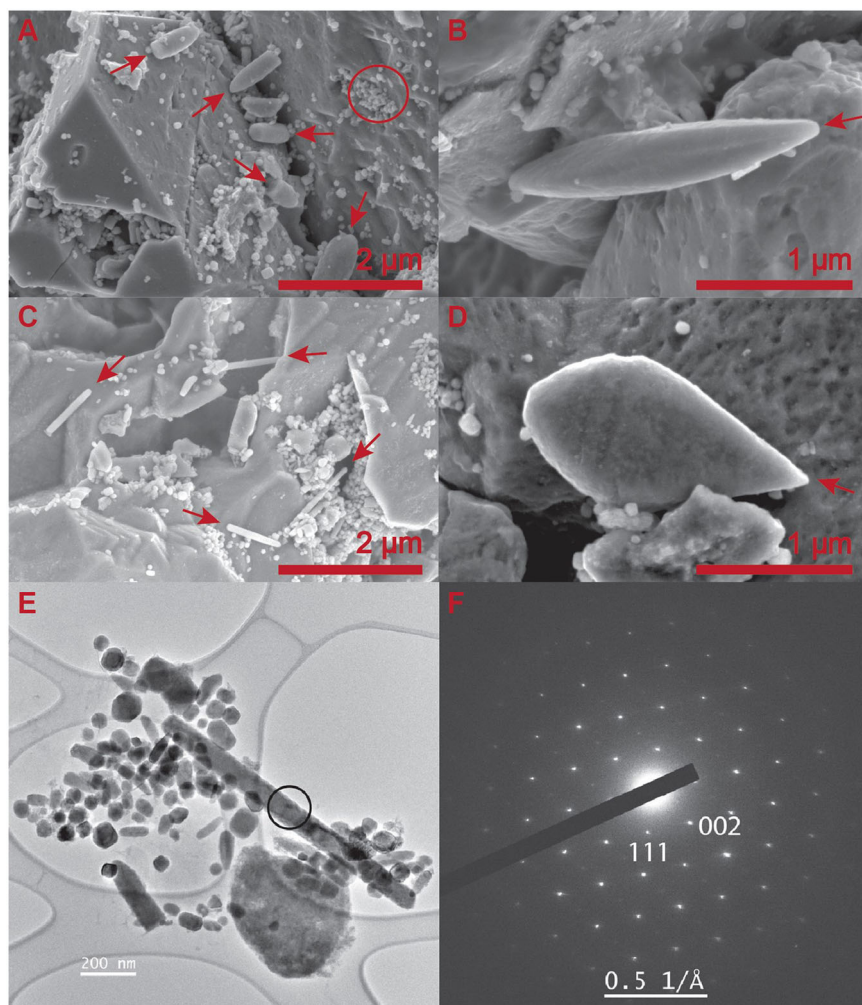
magnetofossils across all eight intervals (e.g., >95% conventional magnetofossils in all cases); therefore, we made separate comparisons for the giant magnetofossils that only include giant magnetofossil morphologies (Table S6). The relative abundance of giant bullets and spearheads decreases while spindles, needles, seeds, squash and spades increase after OAE2.

Discussion

In addition to our study, giant magnetofossils were recently reported within marine sediments spanning the ~93 Ma–1.8 ka interval[27,33,34], adding to prior work that solely documented giant magnetofossils from Palaeocene and Eocene sediments[28,30,32]. Notably, these studies come ~16 years after the first discovery of giant magnetofossils[30]. The scarce number of reported giant magnetofossil findings over this time limits our understanding of these particles. New reports greatly improve our understanding of the ecological distribution of giant magnetofossils in the geologic record, but we are still stymied by a lack of a modern analogue. Similarly, although metagenomic studies suggest that magnetotactic bacteria may have evolved in the Archaean[18], the conventional magnetofossil record only goes back to the mid-Cretaceous[26,27]. Here we show a robust, well-preserved record of both conventional and giant magnetofossils with high abundance and disparity from mid-Cretaceous sediments preceding the Cretaceous-Palaeogene mass extinction event. These observations demonstrate the resilience of iron biomineralizing organisms that produce magnetofossils. Furthermore, consistent shapes and morphologies with younger magnetofossils (Fig. 6) suggest that Cretaceous organisms occupied similar niches with similar ecological preferences.

Magnetofossil identification and discovery of potentially new giant magnetofossil morphologies

Conventional magnetofossils are magnetically single domain because magnetotactic bacteria, the organisms that make them, optimise these particles for navigating chemical gradients within the water column[1–5]. Although we do not know how giant needle-shaped magnetofossils were made, they are also single domain[57] and, therefore, may have been used for a similar navigational function as conventional magnetofossils[28,31,57]. On the other hand, giant bullets, spearheads, and spindles are expected to have vortex or multidomain behaviour unless they are preserved in chains[28,57]. These observations have led to the interpretation that giant bullets, spearheads, and spindles were used for an alternative function, such as a feeding apparatus, defensive armour, or a shuttling mechanism[29–31].

The standard conventional magnetofossil crystals (e.g., cuboctahedra, bullets and prismatic) imaged in this study have compositions, shapes, and size ranges consistent with reported, younger single-domain magnetite magnetofossils (Figs. S5–S16)[20,31]. Similarly, the standard giant magnetofossil crystals (bullets, spindles, needles, and spearheads) imaged in this study have compositions, shapes, size ranges, and predicted magnetic domain states consistent with reported, younger giant magnetite magnetofossils (Figs. 6, S5–S15 and S17–S20)[30–32,57]. The three potentially new giant magnetofossil categories reported here (e.g., seed, squash, and spades) have iron oxide compositions consistent with magnetite and, like giant bullets, spindles, and spearheads, are predicted to be in the magnetic vortex or multidomain states based on their shapes and dimensions (Figs. 6, S21–S23 and S25–S27).

Fig. 5 | Electron micrographs of magnetofossils from the post-OAE2 interval. A SEM image of giant bullets from HP30465. **B** SEM image of spindles from HP31425. **C** SEM image of a needle from HP31435. **D** SEM image of a spearhead from HP31435 with a pronounced groove bisecting the widest part of the crystal. **E** Transmission electron microscope image of conventional magnetofossils and a small needle from HP31375. **F** SAED pattern for the needle magnetofossil in (**E**) with the [−1−1−1], [3−1−1] and [1−1−1] magnetite directions labelled. The red arrows in panels **A**–**D** point to giant magnetofossils. An example of the conventional magnetofossils observed in the SEM images is highlighted by the red circle in panel (**C**).
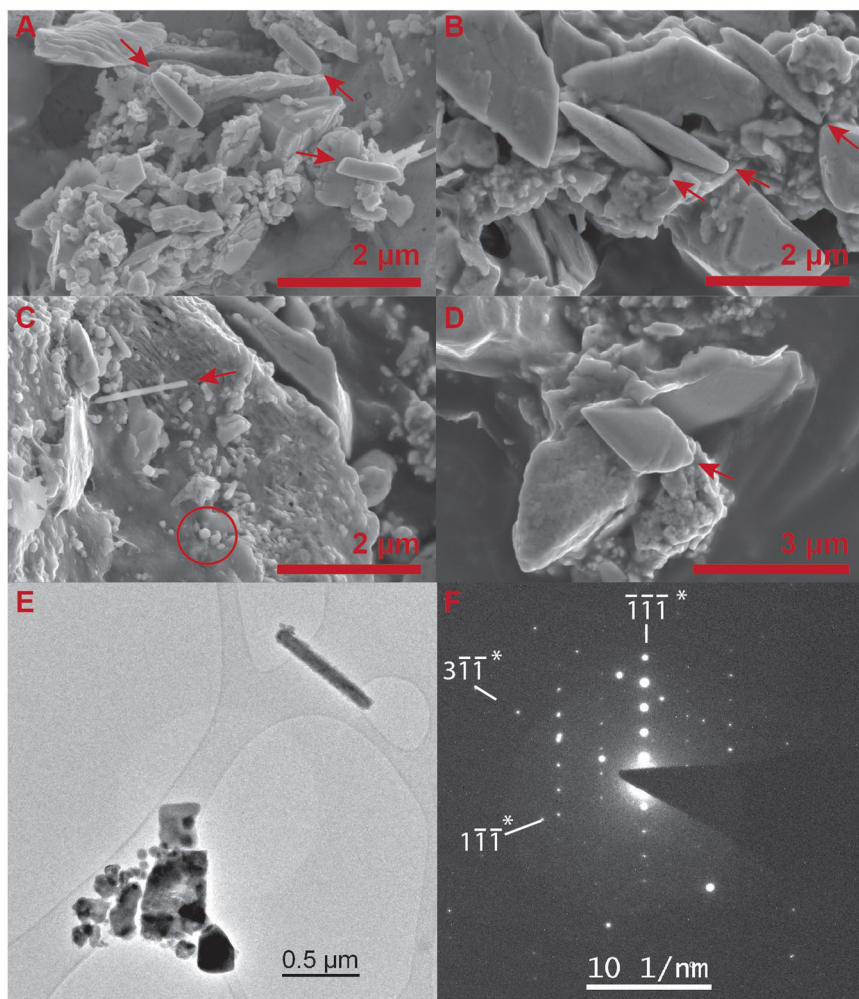
The presumptive seed giant magnetofossils have consistent hexoctahedral crystal habits and, unlike most of the other giant magnetofossil categories, have a tight linear relationship between length and width ($R^2 = 0.89$, Fig. 6, S21 and S25) which suggests that they grow along a size continuum. Notably, similar relationships are observed during different growth stages of anisotropic, conventional bullet shapes[58,59]. If the seed particles are biogenic, the similarity in crystal habit to conventional cuboctahedral magnetofossils, albeit elongated, may indicate that the GIBO that biomineralized giant seeds and magnetotactic bacteria that produce cuboctahedra-shaped particles share a common ancestor or environmental preferences. Although we only identified two putative squash giant magnetofossils (Figs. S22 and S26), their distinct characteristics also suggest that they are biogenic. For example, both particles have stalk-like endings, which have, to our knowledge, only been observed in spearheads (these forms have not yet been documented from abiotic sources). They also have unusual surface textures, which could be a diagenetic feature, but resemble dimpled textures sometimes observed on spearheads.

Xue et al.[32] suggested that the planes segmenting spearheads constitute evidence for the biogenicity of these magnetofossil morphologies. These planes correspond to the [220] crystal plane in magnetite, which spearheads often seem to break along. Although the spade-like crystals have similar habits to spearheads, we did not observe these segmentations on any spade particles, nor did we observe any surface textures (Fig. S23). According to Xue et al.[32], our observations indicate that the spade-like crystals are distinct from spearheads and, if they are biogenic, they were likely made by different organisms. This does not discount the possibility that the GIBO that biomineralized spade and spearhead morphologies are related or that they biomineralized these particles for a similar function (e.g., perhaps both organisms used these particles as a form of protective armour). Further documentation (e.g., crystallographic studies, micromagnetic modelling and isotopic analyses) of giant spades, seeds, and squash in other sedimentary records will help to confirm their biogenicity. Under-sampling and/or extinction of the GIBO that made these unusual shapes, perhaps during the Cretaceous-Palaeogene mass extinction event, are potential reasons why these shapes have not yet been reported.

Differences in preservation between conventional and giant magnetofossils

Conventional magnetofossil abundance decreased substantially after OAE2, whereas there is no obvious difference in giant magnetofossil abundance after OAE2 (Tables S1–S6). The large conventional magnetofossil decrease caused the giant magnetofossil percent magnetite volume to increase from ~51.5% to ~98.1% (Tables S7 and S8). The relative abundance of conventional cuboctahedral magnetofossils also decreased with respect to the relative abundance of bullet shapes (Table S5). Coincident with these changes is the appearance in SEM images of a film on magnetically extracted material from the post-OAE2 interval (Fig. S28). There is also a lithologic difference between the pre- and post-OAE2 intervals, from silty clay to laminated sand (Fig. 2). There are no noticeable differences in signal or central ridge contributions between the pre- and post-OAE2 FORC datasets (Fig. 3).

Taken together, these observations suggest a notable sediment and/or water chemistry change between the pre- and post-OAE2 intervals. This
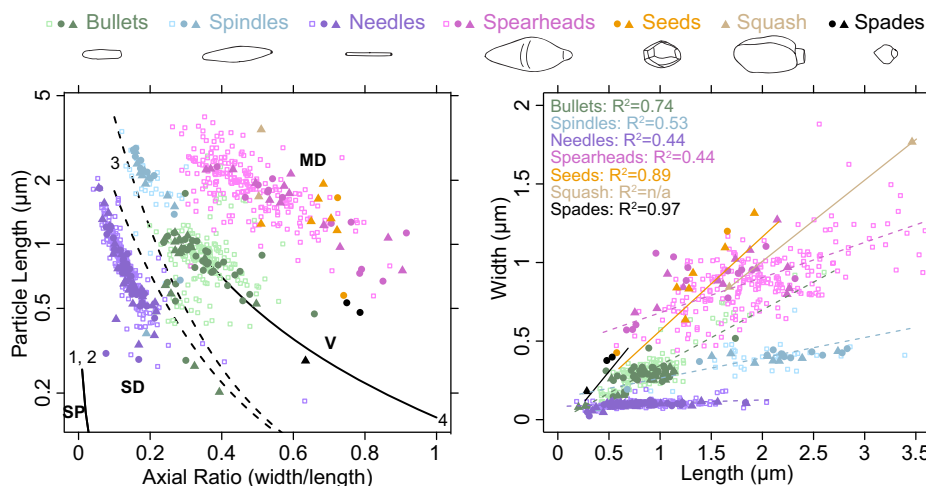
Fig. 6 | Giant magnetofossil dimensional analyses. Left panel: Modified Butler-Banerjee plot of giant magnetofossils. The bottom solid line, labelled 1 and 2, represents the limit for six-crystal magnetofossil chains with intercrystal gaps of 1 and 0.6 times the length of constituent crystals[78], and the lower limit for isolated single domain particles[79]. The dashed lines in the middle of the plot, labelled 3, represent the upper limits for isolated single-domain particles with long axes parallel to the [100] (left line) and [111] (right line) crystallographic axes[80]. The solid line, labelled 4, is the critical size for isolated crystals within a chain of three crystals[80]. SP is superparamagnetic, SD is single domain, V is vortex and MD is multidomain. Right panel: Width-length comparisons of giant magnetofossils. Dashed lines are the linear regressions for each giant magnetofossil group and include measurements of Cretaceous, Palaeocene and Eocene giant magnetofossils. The solid lines are the regression lines for the putative giant seed magnetofossils and a standard line connecting the two putative squash particles (there are not enough data points for a linear regression) identified in this study. In both panels, Cretaceous giant magnetofossils from this study are denoted with solid symbols and Palaeocene-Eocene giant magnetofossils from previous studies are denoted with open symbols[30–32]. Solid circles are from intervals below Oceanic Anoxic Event 2 (pre-OAE2), and solid triangles are from intervals above OAE2 (post-OAE2). Giant bullets are represented by green symbols, spindles by blue, needles by purple, spearheads by pink, seeds by orange, squash by brown, and spades by black symbols. Simple cartoons across the top of the figure represent each of these morphologies. The cartoons are approximately scaled to one another and placed such that their presumed magnetically easy axes/growth directions are oriented from left to right.

sediment-water chemistry difference over the post-OAE2 interval can be explained by two potential scenarios. In the first, the post-OAE2 interval is dominated by a change in baseline environmental conditions following the OAE2 event (i.e., during magnetofossil deposition). In this scenario, MTB would have been more 'stressed' by environmental conditions, producing less abundant magnetofossils, while also selecting for MTB that produce bullet shapes. GIBO, on the other hand, would have been unaffected and/or better adapted to survive these new environmental conditions and remained unchanged. In the second scenario, the post-OAE2 record was more susceptible to diagenesis than the pre-OAE2 record (i.e., after magnetofossil deposition). In this scenario, magnetofossil assemblage changes could represent a change to conditions that were less conducive to conventional magnetofossil preservation. It is also possible that the film observed in our SEM images somehow inhibited magnetic extraction, which would explain why there are no discernable differences between the FORC datasets. The lack of changes observed in the giant magnetofossil assemblages is consistent with the interpretation that they are more resistant to diagenesis, possibly because of their size. Importantly, this observation does not rule out the likelihood that they were also affected by dissolution, which produced a smaller sample size. In summary, we argue that, regardless of the explanation, this is evidence that giant magnetofossils may be better preserved in the sedimentary record when present than conventional magnetofossils.

Although we cannot rule out diagenesis as an explanation for the large difference in conventional magnetofossil abundances from the pre- to post-OAE2 intervals, it is likely that all conventional magnetofossil morphologies experienced the same amount of diagenesis within each interval (i.e., no preferential dissolution of specific particle morphologies in each sample). Thus, we can compare relative conventional magnetofossil abundances between these intervals. The most notable differences are the decrease in cuboctahedra and the increase in small bullets after OAE2, which is consistent with increased seasonal stratification and more nutrient/organic-rich conditions typically spurred by increased seasonality[60]. These conditions are often linked to warmer global temperatures that lead to increased precipitation and terrestrial runoff, as supported by the lithology change at

Holland Park and on the nearby North Carolina Coastal Plain over this time period[36]. Small increases in medium and large bullets after OAE2 further support this interpretation because a similar trend was observed within nearby continental shelf sediments that record the Palaeocene-Eocene Thermal Maximum[31,61]. In this example, an increase in bullet-shaped conventional magnetofossils and low-oxygen tolerant benthic foraminifera were interpreted together to represent seasonal water column stratification, organic matter, and nutrient supply associated with a baseline seasonality increase during the Palaeocene-Eocene Thermal Maximum.

Ecological changes recorded by magnetofossils

Unlike the conventional magnetofossil assemblages, the total number of giant magnetofossils counted within the pre- and post-OAE2 intervals is similar ($n = 85$ and $n = 88$, respectively) (Table S4). However, the overall number of conventional magnetofossils is still much greater than the number of giant magnetofossils within each interval ($n = 15,716$ and $n = 3140$, respectively) so it is easier to observe giant magnetofossil changes by looking at the relative abundances of each of the giant magnetofossil morphology (Table S6). The most notable difference is a large decrease in giant bullets (−20.5%) from the pre- to post-OAE2 interval. This change is accompanied by a smaller decrease in spearheads (−7.5%) and an increase in spindles (+6.7%), needles (+7.5%), seeds (+9.9%), squash (+3.6) and spades (+0.3%). Notably, the large giant bullet decrease is coincident with the overall increase in conventional bullet shapes. For example, samples HP40624 and HP31375 have the lowest giant bullet percentages (11.1% and 0%, respectively) but comparatively, these samples have some of the highest small (28.3% and 27.8%) and medium conventional bullet percentages (7.5% and 7.7%) compared to other samples. Concurrent changes within the conventional and giant magnetofossil assemblages support the interpretation that GIBO behave similarly to magnetotactic bacteria, in that both GIBO and magnetotactic bacteria may have specific ecological preferences and produce differently shaped magnetofossils depending on environmental conditions or water column position (e.g. [60,62–68]). Future work should compare robust giant magnetofossil assemblages to one another
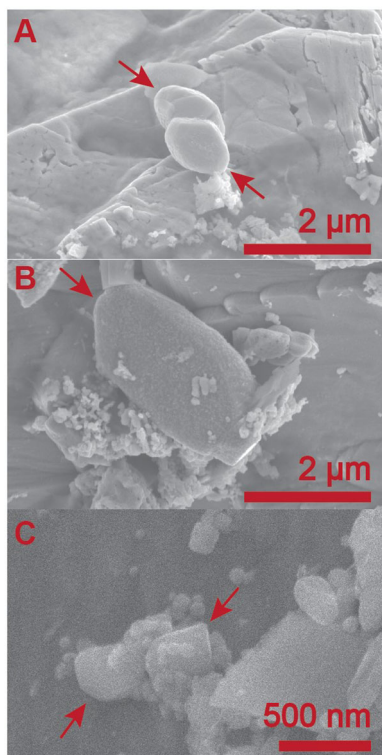
Fig. 7 | Scanning electron micrographs of potentially new giant magnetofossil morphologies. The 'new', possible magnetofossil shapes are indicated by red arrows in each image. **A** Two particles with hexoctahedral habit. The crystal edges are slightly rounded with ~1.35 μm average size. We refer to these putative magnetofossil shapes as "seeds." **B** One particle with a prolate crystal shape tapers slightly on one end, while the wider end contains a short stalk. These putative magnetofossil shapes are an average of ~2.57 μm; we refer to them as "squash." **C** Two particles with average size of ~0.43 μm; we refer to them as "spades." Energy dispersive X-ray spectra indicate that these particle morphologies have iron oxide compositions consistent with magnetite (Supplemental Information).

from well-studied and well-documented sediment archives to better understand the environmental changes that drive giant magnetofossil disparity.

A case for widespread giant magnetofossil distribution in the rock record

Prior to recent work, giant magnetofossils were only identified within and around major carbon cycle perturbations[28,30,32] which led to the interpretation that they are associated with environmental changes exacerbated by these warm periods. Recent reports[27,33], including this study, demonstrate that giant magnetofossils are more widely distributed in the geologic record. It is possible that they have not been identified due to under-sampling. For example, although the giant magnetofossils reported here are well preserved, perhaps better preserved than the conventional magnetofossils, they occur in much lower proportions than the conventional magnetofossil assemblages (e.g., they comprise <4.3% of total magnetofossils in all scenarios). Interestingly, even when there are so few giant magnetofossils compared to conventional magnetofossils, they can contribute significantly to the percent magnetite volume (Tables S7 and S8).

In practice, because of the stable single-domain nature of giant needle-shaped magnetofossils, the biogenic needle component can be used to 'remotely detect' giant needles and other giant magnetofossils by association[57]. However, as seen here, sometimes there is not an obvious biogenic needle component visible (Figs. 3, S3 and S4), but there are still features consistent with the presence of single domain magnetite, or

conventional magnetofossils[52,53]. As such, we highlight the need for careful, thorough sampling and electron microscopy analyses, especially on samples containing magnetic signatures consistent with conventional magnetofossils, to increase the chances of imaging giant magnetofossils and accurately identifying their presence.

In summary, we report the oldest robust conventional and giant magnetofossil record from outer neritic Cenomanian sediments, at ~97 Ma. Magnetofossils from both the Cenomanian and Turonian intervals at Holland Park are abundant and have high morphological disparity. Together, with other recent studies by Kadam et al.[33] and Xue and Chang[27], these findings highlight the robustness and potential widespread distribution of both MTB and GIBO within sediments spanning the geologic record.

Materials and methods

The Holland Park core was drilled by the Virginia Department of Environmental Quality in the City of Suffolk, Virginia, at latitude/ longitude N36° 40' 55.6"; W76° 46' 50.1" (NAD 83) and land surface elevation of 23.9 m, in 2012. Core was described visually by onsite geologists using hand lenses. Approximately 139 m of core was recovered; here we focus on the portion of the core between 126.0 and 81.4 m, which records the Cenomanian-Turonian transition and Oceanic Anoxic Event 2 (OAE2).

Biostratigraphy

Sixty-seven samples from 138.4 to 83.4 m were collected and analysed for calcareous nannofossil content from the central portion of the core to avoid contamination from the drilling fluid (Supplementary Data 1). Smear slides were made using the standard technique of Bown and Young[69] for sandy samples and the technique of Shamrock et al.[70] and Shamrock et al.[71] for samples high in total organic carbon and mounted using Norland Optical Adhesive 61, at the United States Geological Survey, Florence Bascom Center. The zonations of Sissingh[43] and Burnett[44] were used to assign ages and were correlated to the timescale of Gradstein et al.[72]. An expanded stratigraphic column, with nannofossil zones, is included in the Supplemental Information.

Total organic carbon and carbon isotopes

Eighty-three samples from the Holland Park core were analysed for total organic carbon and organic carbon isotopes ($\delta^{13}C_{org}$) using the methods of Oliver and Warden[73] and Révész et al.[74], respectively (Supplementary Data 1). Samples were analysed at the United States Geological Survey, Central Energy Resources Science Center and Denver Federal Center. These data were used to further constrain the OAE2 record in the Holland Park core.

Hysteresis loops, backfield curves and first-order reversal curve (FORC) measurements

We measured the bulk magnetic properties of 103 specimens spanning the entire interval of interest (126.0-81.4 m) to determine whether magnetic minerals were present, including magnetofossils. Hysteresis loops and backfield curves were measured for each specimen to determine M_s, M_r, B_c, B_{cr} and their interparametric ratios (M_r/M_s and B_{cr}/B_c; Supplementary Data 1). We then used these parameters to select 26 specimens for FORC measurement[75]: 15 specimens from sediments within the pre-OAE2 Cenomanian interval (spanning 124.4–118.0 m), two from sediments within the OAE2 interval (from 115.1 m and 107.0 m), seven from sediments within the post-OAE2 Turonian interval (spanning 95.8–92.9 m), and one each from the bottom (125.2 m) and top (90.0 m) sediments of the interval of interest. All magnetic measurements were made using an 8604 Lake Shore vibrating sample magnetometer at the Biogeomagnetism Laboratory, National Museum of Natural History, Smithsonian Institution. More measurement details and processing protocols can be found within the Supplemental Information.

Magnetic extracts and electron microscopy

Eight stratigraphic horizons were selected for electron microscopy imaging from the magnetically subdivided pre-OAE2 Cenomanian (124.4–118.0 m) and post-OAE2 Turonian sediment intervals of interest (95.8–92.3 m) to determine whether magnetofossils are the source of the single domain magnetite signatures observed in the FORC datasets[54]. We created magnetic extracts from samples HP40825 (124.4 m), HP40625 (123.8 m), HP39705 (121.0 m), HP38715 (118.0 m), HP31435 (95.8 m), HP31375 (95.6 m), HP30900 (94.2 m) and HP30465 (92.9 m) following the modified protocol of Strehlau et al.[76] by Wagner et al.[31]. Additionally, we selected two horizons outside of the sediment intervals of interest, HP35110 (107.02 m) and HP29530 (90.01 m), to confirm the absence of magnetofossils. Magnetic extracts were created using the same methods as for the sediment intervals of interest.

A subset of each magnetic mineral extract was prepared for scanning electron microscope (SEM) imaging by pipetting two drops of material onto an SEM stub (with carbon tape), air drying the samples inside a desiccation chamber, and applying a 15 nm carbon coating. We randomly acquired ~15 SEM images for each sample at ~69,000× magnification and a horizontal field width of six μm. These images were used to determine the relative magnetofossil morphology proportions per horizon and to estimate per cent magnetite volume (Supplementary Data 1). Higher magnification images and energy dispersive spectroscopy (EDS) analyses were acquired on areas containing densely packed conventional magnetofossils and at least one giant bullet, spindle, needle, spearhead, seed, squash, and spade to confirm magnetofossil iron oxide mineralogy. SEM analyses were performed on the Thermo-FEI Quattro SEM within the Department of Mineral Sciences, National Museum of Natural History, Smithsonian Institution. EDS spectra were acquired using two opposed Thermo EDS detectors with an accelerating voltage of 15 kV. Compositions were determined using the Pathfinder EDS element peak library.

The remaining magnetically extracted material was used to prepare transmission electron microscope (TEM) grids for samples HP40825, HP40625, HP31435 and HP31375. For each sample, a drop of magnetic extract was pipetted onto a TEM grid and then air-dried inside a desiccation chamber. TEM images were acquired randomly, and SAED patterns were collected on representative areas to determine the mineralogy of the magnetic particles. TEM analyses were performed using the JEOL F200 Cold FEG TEM and TECNAI TF30 scanning TEM at the Materials Characterisation and Processing facility at Johns Hopkins University using accelerating voltages between 200 and 300 keV. We used the Gatan GMS 3 Digital Micrograph Software to count and measure magnetofossil dimensions (in SEM and TEM images) and to measure d-spacings on high-resolution TEM images. We used the same software to rotationally average SAED patterns collected during TEM analyses. CrystalMaker and CrystalDiffract were then used to identify the crystallographic axes of magnetite.

Data availability

The datasets presented in this paper are available in the supporting information Word document and Excel file, which are available on figshare.com. The corresponding author may also be contacted for files, directly.

References

1. Frankel, R. B., Blakemore, R. P. & Wolfe, R. S. Magnetite in freshwater magnetotactic bacteria. *Science* **203**, 1355–1356 (1979).
2. Farina, M., Esquivel, D. M. S. & de Barros, H. G. P. L. Magnetic iron-sulphur crystals from a magnetotactic microorganism. *Nature* **343**, 256–258 (1990).
3. Bazylinski, D. A., Garratt-Reed, A. J. & Frankel, R. B. Electron microscopic studies of magnetosomes in magnetotactic bacteria. *Microsc. Res. Tech.* **27**, 389–401 (1994).
4. Bazylinski, D. A. et al. Controlled biomineralization of magnetite (Fe_3O_4) and greigite (Fe_3S_4) in a magnetotactic bacterium. *Appl. Environ. Microbiol.* **61**, 3232–3239 (1995).
5. Bazylinski, D. A. & Frankel, R. B. Magnetosome formation in prokaryotes. *Nat. Rev. Microbiol.* **2**, 217–230 (2004).
6. Amor, M., Tharaud, M., Gélabert, A. & Komeili, A. Single-cell determination of iron content in magnetotactic bacteria: implications for the iron biogeochemical cycle. *Environ. Microbiol.* **22**, 823–831 (2020).
7. Chen, A. P. et al. Magnetic properties of uncultivated magnetotactic bacteria and their contribution to a stratified estuary iron cycle. *Nat. Commun.* **5**, 1–11 (2014).
8. Lin, W., Bazylinski, D. A., Xiao, T., Wu, L. F. & Pan, Y. Life with compass: diversity and biogeography of magnetotactic bacteria. *Environ. Microbiol.* **16**, 2646–2658 (2014).
9. Lin, W., Pan, Y. & Bazylinski, D. A. Diversity and ecology of and biomineralization by magnetotactic bacteria. *Environ. Microbiol. Repts* **9**, 345–356 (2016).
10. Lin, W. et al. Expanding magnetic organelle biogenesis in the domain Bacteria. *Microbiome* **8**, 1–28 (2020).
11. Li, J. et al. Intracellular silicification by early-branching magnetotactic bacteria. *Sci. Adv.* **8**, 1–13 (2022).
12. Li, J., Liu, P., Wang, J., Roberts, A. P. & Pan, Y. Magnetotaxis as an adaptation to enable bacterial shuttling of microbial sulfur and sulfur cycling across aquatic oxic-anoxic interfaces. *J. Geophys. Res. Biogeosci.* **125**, e2020JG006012 1–17 (2020).
13. Li, J. et al. Diverse intracellular inclusion types within magnetotactic bacteria: implications for biogeochemical cycling in aquatic environments. *J. Geophys. Res. Biogeosci.* **126**, 1–19 (2021).
14. Amor, M., Mathon, F. P., Monteil, C. L., Busigny, V. & Lefevre, C. T. Iron-biomineralizing organelle in magnetotactic bacteria: function, synthesis and preservation in ancient rock samples. *Environ. Microbiol.* **22**, 3611–3632 (2020).
15. Roberts, A. P. et al. Magnetotactic bacterial abundance in pelagic marine environments is limited by organic carbon flux and availability of dissolved iron. *Earth Planet. Sci. Lett.* **310**, 441–452 (2011).
16. Goltsman, D. S. A. A., Comolli, L. R., Thomas, B. C. & Banfield, J. F. Community transcriptomics reveals unexpected high microbial diversity in acidophilic biofilm communities. *ISME J.* **9**, 1014–1023 (2015).
17. Abreu, F. et al. Culture-independent characterization of a novel uncultivated magnetotactic member of the Betaproteobacteria class of the Proteobacteria phylum from an acidic lagoon. *Environ. Microbiol.* **20**, 2615–2624 (2018).
18. Lin, W. et al. Origin of microbial biomineralization and magnetotaxis during the Archean. *Proc. Natl. Acad. Sci. USA* **114**, 2171–2176 (2017).
19. Moskowitz, B. M., Frankel, R. B. & Bazylinski, D. A. Rock magnetic criteria for the detection of biogenic magnetite. *Earth Planet. Sci. Lett.* **120**, 283–300 (1993).
20. Kopp, R. E. & Kirschvink, J. L. The identification and biogeochemical interpretation of fossil magnetotactic bacteria. *Earth Sci. Rev.* **86**, 42–61 (2008).
21. Chang, S. B. R. Magnetofossils, the magnetization of sediments, and the evolution of magnetite biomineralization. *Annu. Rev. Earth Planet. Sci.* **17**, 169–195 (1989).
22. Akai, J., Iida, A. & Chiba, A. Mn and Fe minerals of possible biogenic origin from two Precambrian stromatolites in Western Australia. *J. Geol. Soc. Jpn* **103**, 484–488 (1997).
23. Thomas-Keprta, K. L. et al. Elongated prismatic magnetite crystals in ALH84001 carbonate globules: potential Martian magnetofossils. *Geochim. Cosmochim. Acta* **64**, 4049–4081 (2000).
24. Li, J., Benzerara, K., Bernard, S. & Beyssac, O. The link between biomineralization and fossilization of bacteria: insights from field and experimental studies. *Chem. Geol.* **359**, 49–69 (2013).

25. Jimenez-Lopez, C., Romanek, C. S. & Bazylinski, D. A. Magnetite as a prokaryotic biomarker: a review. *J. Geophys. Res. Biogeosci.* **115**, 1–19 (2010).
26. Montgomery, P., Hailwood, E. A., Gale, A. S. & Burnett, J. A. The magnetostratigraphy of Coniacian-Late Campanian chalk sequences in southern England. *Earth Planet. Sci. Lett.* **156**, 209–224 (1998).
27. Xue, P. & Chang, L. Spatiotemporal distribution of giant magnetofossils holds clues to their biological origin. *Geol.* **52**, 453–457 (2024).
28. Chang, L. et al. Giant magnetofossils and hyperthermal events. *Earth Planet. Sci. Lett.* **351–352**, 258–269 (2012).
29. Kopp, R. E. et al. An Appalachian Amazon? Magnetofossil evidence for the development of a tropical river-like system in the mid-Atlantic United States during the Paleocene-Eocene thermal maximum. *Paleoceanography* **24**, PA4211 1–PA421117 (2009).
30. Schumann, D. et al. Gigantism in unique biogenic magnetite at the Paleocene-Eocene Thermal Maximum. *Proc. Natl Acad. Sci. USA* **105**, 17648–17653 (2008).
31. Wagner, C. L. et al. Diversification of iron-biomineralizing organisms during the Paleocene-Eocene Thermal Maximum: Evidence from quantitative unmixing of magnetic signatures of conventional and giant magnetofossils. *Paleoceanogr. Paleoclim.* **36**, 1–25 e2021PA004225 (2021).
32. Xue, P., Chang, L., Pei, Z. & Harrison, R. J. Discovery of giant magnetofossils within and outside of the Palaeocene-Eocene Thermal Maximum in the North Atlantic. *Earth Planet. Sci. Lett.* **584**, 117417 (2022).
33. Kadam, N. et al. Discovery of late quaternary giant magnetofossils in the Bay of Bengal. *Commun. Earth Environ.* **5**, 1–12 (2024).
34. Sun, Q. et al. Magnetic fingerprints for the paleoenvironmental evolutions since the Last Deglaciation: evidence from the northwestern South China Sea sediments. *Paleoceanogr. Paleoclim.* **39**, 1–15 (2024).
35. Aleman Gonzalez, W. B. et al. Depositional sequence stratigraphy of Turonian to Santonian sediments, Cape Fear Arch, North Carolina Coastal Plain, USA. *Stratigraphy* **17**, 293–314 (2020).
36. Lowery, C. M., Self-Trail, J. M. & Barrie, C. D. Enhanced terrestrial runoff during Oceanic Anoxic Event 2 on the North Carolina Coastal Plain, USA. *Clim. Past* **17**, 1227–1242 (2021).
37. Gohn, G. S. Revised nomenclature, definitions, and correlations for the Cretaceous formations in USGS-Clubhouse Crossroads #1, Dorchester County, South Carolina. *US Geol. Surv. Prof. Pap.* **1518**, 1–39 (1992).
38. Balson, A. E., Self-Trail, J. & Terry, D. O. The Sunny Point Formation: a new Upper Cretaceous subsurface unit in the Carolina Coastal Plain. *Southeast Geol.* **50**, 1–16 (2013).
39. Weems, R. E., Self-Trail, J. & Edwards, L. E. *Cross section of the North Carolina coastal plain from Enfield through Cape Hatteras. U.S. Geological Survey Open-File Report* https://doi.org/10.3133/ofr20191145 (2019).
40. Valentine, P. C. *Turonian (Eaglefordian) stratigraphy of the Atlantic Coastal Plain and Texas. U.S. Geological Survey Professional Paper* https://doi.org/10.3133/pp1315 (1984).
41. Miller, K. G. et al. Upper Cretaceous sequences and sea-level history, New Jersey Coastal Plain. *Bull. Geol. Soc. Am.* **116**, 368–393 (2004).
42. Sugarman, P., Miller, K., Browning, J., McLaughlin, J. & Kulhanek, D. Late Cretaceous (Turonian-Coniacian) sequence stratigraphy, sea level, and deltaic facies, Magothy Formation, U. S. Middle Atlantic Coastal Plain. *Stratigraphy* **18**, 1–27 (2021).
43. Sissingh, W. Biostratigraphy of Cretaceous calcareous nannoplankton. *Geol. Mijnb.* **56**, 37–65 (1977).
44. Burnett, J. A., Gallagher, L. T. & Hampton, M. J. Upper Cretaceous. in *Calcareous Nannofossil Biostratigraphy* 132–199 (Springer, Netherlands, 1998).
45. Corbett, M. J., Watkins, D. K. & Pospichal, J. J. A quantitative analysis of calcareous nannofossil bioevents of the Late Cretaceous (Late Cenomanian-Coniacian) Western Interior Seaway and their reliability in established zonation schemes. *Mar. Micropaleontol.* **109**, 30–45 (2014).
46. Martini, E. Standard tertiary and quaternary Calcareous Nannoplankton Zonation. *Proc. 2nd Planktonic Conference, Roma.* 739–785 (1971).
47. Scholle, P. A. & Arthur, M. A. Carbon isotope fluctuations in Cretaceous pelagic limestones: potential stratigraphic and petroleum exploration tool. *Am. Assoc. Pet. Geol. Bull.* **64**, 67–87 (1980).
48. Arthur, M. A., Schlanger, S. O. & Jenkyns, H. C. The Cenomanian-Turonian Oceanic Anoxic Event, II. Palaeoceanographic controls on organic-matter production and preservation. *Geol. Soc. Spec. Publ.* **26**, 401–420 (1987).
49. Jenkyns, H. C. Geochemistry of oceanic anoxic events. *Geochem. Geophys. Geosyst.* **11**, 1–30 (2010).
50. Owens, J. D. et al. Patterns of local and global redox variability during the Cenomanian–Turonian Boundary Event (Oceanic Anoxic Event 2) recorded in carbonates and shales from central Italy. *Sedimentology* **64**, 168–185 (2017).
51. Day, R., Fuller, M. & Schmidt, V. A. Hysteresis properties of titanomagnetites: grain-size and compositional dependence. *Phys. Earth Planet. Inter.* **13**, 260–267 (1977).
52. Heslop, D., Roberts, A. P. & Chang, L. Characterizing magnetofossils from first-order reversal curve (FORC) central ridge signatures. *Geochem. Geophys. Geosyst.* **15**, 2170–2179 (2014).
53. Roberts, A. P. et al. Searching for single domain magnetite in the 'pseudo-single-domain' sedimentary haystack: implications of biogenic magnetite preservation for sediment magnetism and relative paleointensity determinations. *J. Geophys. Res. Solid Earth* **117**, 1–26 (2012).
54. Egli, R., Chen, A. P., Winklhofer, M., Kodama, K. P. & Horng, C.-S. Detection of noninteracting single domain particles using first-order reversal curve diagrams. *Geochem. Geophys. Geosyst.* **11**, 1525–2027 (2010).
55. Pósfai, M., Lefèvre, C. T., Trubitsyn, D., Bazylinski, D. & Frankel, R. Phylogenetic significance of composition and crystal morphology of magnetosome minerals. *Front. Microbiol.* **4**, 1–15 (2013).
56. Devouard, B. et al. Magnetite from magnetotactic bacteria: size distributions and twinning. *Am. Mineral.* **83**, 1387–1398 (1998).
57. Wagner, C. L. et al. In situ magnetic identification of giant, needle-shaped magnetofossils in Paleocene-Eocene Thermal Maximum sediments. *Proc. Natl Acad. Sci. USA* **118**, 1–44 e2018169118 (2021).
58. Li, J. et al. Crystal growth of bullet-shaped magnetite in magnetotactic bacteria of the Nitrospirae phylum. *J. R. Soc. Interface* **12**, 1–11 (2015).
59. Li, J. et al. Bullet-shaped magnetite biomineralization within a magnetotactic deltaproteobacterium: implications for magnetofossil identification. *J. Geophys. Res. Biogeosci.* **125**, 1–16 (2020).
60. Egli, R. Characterization of individual rock magnetic components by analysis of remanence curves, 1. Unmixing natural sediments. *Stud. Geophys. Geodyn.* **48**, 391–446 (2004).
61. Wagner, C. L., Stassen, P., Thomas, E., Lippert, P. C. & Lascu, I. Magnetofossils and benthic foraminifera record changes in food supply and deoxygenation of the coastal marine seafloor during the Paleocene-Eocene Thermal Maximum. *Paleoceanogr. Paleoclim.* **37**, e2022PA004502 (2022).
62. Petermann, H. & Bleil, U. Detection of live magnetotactic bacteria in South Atlantic deep-sea sediments. *Earth Planet. Sci. Lett.* **117**, 223–228 (1993).
63. Yamazaki, T. & Kawahata, H. Organic carbon flux controls the morphology of magnetofossils in marine sediments. *Geology* **26**, 1064–1066 (1998).

64. Moskowitz, B. M., Bazylinski, D. A., Egli, R., Frankel, R. B. & Edwards, K. J. Magnetic properties of marine magnetotactic bacteria in a seasonally stratified coastal pond (Salt Pond, MA, USA). *Geophys. J. Int.* **174**, 75–92 (2008).

65. Yamazaki, T. & Shimono, T. Abundant bacterial magnetite occurrence in oxic red clay. *Geology* **41**, 1191–1194 (2013).

66. Chen, A. P. P. et al. Magnetic properties of uncultivated magnetotactic bacteria and their contribution to a stratified estuary iron cycle. *Nat. Commun.* **5**, 1–11 (2014).

67. Rivas-Lamelo, S. et al. Magnetotactic bacteria as a new model for P sequestration in the ferruginous Lake Pavin. *Geochem. Perspect. Lett.* **5**, 35–41 (2017).

68. Yuan, W., Zhou, H., Yang, Z., Hein, J. R. & Yang, Q. Magnetite magnetofossils record biogeochemical remanent magnetization in hydrogenetic ferromanganese crusts. *Geology* **48**, 298–302 (2020).

69. Bown, P. R. & Young, J. R. Techniques. in *Calcareous Nannofossil Biostratigraphy* (ed Bown, P. R.) 16–28 (Chapman and Kluwer Academic, 1998).

70. Shamrock, J. L., Munoz, E. J. & Carter, J. H. An improved sample preparation technique for calcareous nannofossils in organic-rich mudstones. *J. Nannoplankt. Res.* **35**, 101–101 (2015).

71. Shamrock, J. L. & Self-Trail, J. M. Quantification of a pretreatment procedure for organic-rich calcareous nannofossil samples. *Int. Nannoplankt. Assoc.* **36**, 65–75 (2016).

72. Gradstein, F. M., Ogg, J. G., Schmitz, M. D. & Ogg, G. M. *Geologic Time Scale 2020*. (Elsevier, 2020).

73. Oliver, T. & Warden, A. Petroleum Geochemistry Research Laboratory total organic carbon and total carbon method. *U.S. Geol. Surv. Web Page* https://doi.org/10.5066/P9X85HUF (2020).

74. Révész, K., Qi, H. & Coplen, T. B. Determination of the $\delta^{15}N$ and $\delta^{13}C$ of total nitrogen and carbon in solids; RSIL lab code 1832, chap. 5 of Stable isotope-ratio methods, sec. C. in *Methods of the Reston Stable Isotope Laboratory (slightly revised from version 1.1 released in 2007): U.S. Geological Survey Techniques and Methods, book 10* (eds Révész, K. & Coplen, T. B.) 1–31 (2012).

75. Pike, C. R., Roberts, A. P. & Verosub, K. L. Characterizing interactions in fine magnetic particle systems using first order reversal curves. *J. Appl. Phys.* **85**, 6660–6667 (1999).

76. Strehlau, J. H., Hegner, L. A., Strauss, B. E., Feinberg, J. M. & Penn, R. L. Simple and efficient separation of magnetic minerals from speleothems and other carbonates. *J. Sediment. Res.* **84**, 1096–1106 (2014).

77. Roberts, A. P., Heslop, D., Zhao, X. & Pike, C. R. Understanding fine magnetic particle systems through use of first-order reversal curve diagrams. *Rev. Geophys.* **52**, 522–555 (2014).

78. Newell, A. J. Transition to superparamagnetism in chains of magnetosome crystals. *Geochem. Geophys. Geosyst.* **10**, Q11Z08 1–Q11Z0819 (2009).

79. Butler, R. F. & Banerjee, S. K. Theoretical single-domain grain size range in magnetite and titanomagnetite. *J. Geophys. Res.* **80**, 4049–4058 (1975).

80. Muxworthy, A. R. & Williams, W. Critical single-domain/multidomain grain sizes in noninteracting and interacting elongated magnetite particles: implications for magnetosomes. *J. Geophys. Res. Solid Earth* **111**, B12S12 3–B12S12 9 (2006).

Acknowledgements

Author contributions

C.L.W. designed research; C.L.W., I.L., J.M.S.T., T.G., K.J.T.L., G.G., K.G., J.W., M.D. and T.O. performed research; C.L.W., I.L., J.M.S.T., T.G. and K.J.T.L. analysed data; C.L.W. wrote the paper with contributions from I.L., J.M.S.T., T.G. and K.J.T.L; J.M.S.T. provided stratigraphic interpretations; C.L.W. and I.L. provided magnetic interpretations; C.L.W., T.G. and K.J.T.L. provided electron microscopy interpretations.

Competing interests

The authors declare no competing interests.

Additional information

Supplementary information The online version contains supplementary material available at https://doi.org/10.1038/s43247-024-01540-2.

Correspondence and requests for materials should be addressed to Courtney L. Wagner.

Peer review information *Communications Earth & Environment* thanks Andrew Roberts and the other, anonymous, reviewer(s) for their contribution to the peer review of this work. Primary Handling Editor: Joe Aslin. A peer review file is available.

Reprints and permissions information is available at http://www.nature.com/reprints

Publisher's note Springer Nature remains neutral with regard to jurisdictional claims in published maps and institutional affiliations.